COMMUNICATION

Received 00th 20xx,
Accepted 00th 20xx
DOI: 10.1039/x0xx00000x

Stabilization of Cu^+ by engineering CuO-HfO_2 interface toward enhanced CO_2 electroreduction to C_2H_4

Xin Li,[a] Lifen Li,[b] Lijun Wang,[a] Qineng Xia,[b] Leiduan Hao,[a] Xinyu Zhan,[a] Alex W. Robertson[c] and Zhenyu Sun*

We report significantly enhanced electrochemical CO_2 reduction (ECR) to C_2H_4 by tuning the interface of a metal oxide composite (CuO_x/HfO_2), enabling a C_2H_4 faradaic efficiency as high as 62.6 ± 1.3% at 300 mA cm^{-2}, in contrast to only 11.6 ± 1.6% over pure CuO. Collective knowledge from multiple control experiments, density functional theory calculations, and operando Raman study reveals that HfO_2 greatly strengthens CO_2 adsorption and also stabilizes the Cu^+ species during the ECR, thus benefiting binding of *CO for further C–C coupling to yield C_2H_4. This work offers a simple and effective avenue to enhancing the ECR to yield C_2H_4.

Burning of fossil fuels leads to a dramatic increase in CO_2 emission, causing severe climate change.[1] Electrochemical CO_2 reduction (ECR) into fuels and valuable feedstocks powered by renewable electricity, provides a promising route to alleviate global warming and simultaneously close the carbon loop.[2] A plethora of electrocatalysts including metals,[3,4] metal oxides,[5,6] transition metal dichalcogenides,[7,8] metal-organic frameworks,[9,10] and single-atom catalysts[11,12] have been developed for the ECR. Among these materials, Cu-based catalysts are promising for selectivity towards C_{2+} (containing two or more carbon atoms) products due to favourable d-band levels and moderate CO binding energies.[13,14] ECR to ethylene (C_2H_4) is appealing because this compound is highly demanded as a feedstock in industry and is also widely utilized as plant growth regulator for ripening fruits. However, it is still a challenge to efficiently reduce CO_2 to C_2H_4 because of three major obstacles: 1) the occurrence of the more rapid hydrogen evolution reaction (HER) at similar or even lower overpotentials; 2) competition with C–O and C–H bond formation; and 3) the formidable C–C coupling energy barrier.

It's generally surmised that C_2H_4 is obtained through dimerization of a common *CO (* denotes adsorption site) intermediate via the following possible steps 1) *CO → $*C_2O_2$ → *COCOH → $*CH_2CHO$ → C_2H_4; 2) *CO → *CHO → *COCHO → *COCHOH → C_2H_4; 3) *CO → *CHO → *OHCCOH → $*CH_2CHO$ → $*OH_2CCH_2$ → C_2H_4.[15] Under such circumstance, optimizing the binding strength of the *CO intermediate and lowing the *CO coupling barriers as well as concurrently suppressing the excessive H adsorption (to allieviate the parasitic HER and formation of CH_4) are critical to promote CO_2 reduction selectively to C_2H_4. Herein, we demonstrate for the first time facile synthesis of a CuO_x/HfO_2 heterostructure with large and intimate contact interface. HfO_2 is selected to construct the interface by taking advantage of its low cost, outstanding thermal and chemical stability, strong mechanical properties, high surface basicity, and exceptional CO_2 adsorption capability. Of particular interest is that introduction of the reducible HfO_2 can evidently stabilize Cu^+ against its further reduction during electrolysis, thereby remarkably enhancing the ECR yield to C_2H_4. The ECR activity is tunable by adjusting the Cu-to-Hf molar ratio with an optimal value of 3:2, giving rise to a C_2H_4 formation rate of 62.6 ± 1.3% at 300 mA cm^{-2} in a flow reactor, exceeding bare CuO and many previously reported Cu-based catalysts.

The CuO_x/HfO_2 composite catalysts were prepared through a simple hydrothermal method based on the coprecipitation of $Cu(Ac)_2{\cdot}H_2O$ and $HfCl_4$ in alkaline medium. Shown in Fig. 1a and Fig. S1 are the X-ray diffraction (XRD) patterns of CuO_x/HfO_2 with various HfO_2 loadings, along with pure CuO and HfO_2 synthesized in a similar fashion. For CuO_x/HfO_2, the diffraction peaks at ~24.2, 28.4, 31.7, 41, 45.8, 50.4, and 55.6° can be well attributed to the (011), ($\bar{1}$11), (111), ($\bar{2}$11), ($\bar{2}$02), (220), and (221) reflections of monoclinic HfO_2 (JCPDS no.: 078–0049), respectively. Broad and intense diffraction peaks located at ~35.5, 38.7, 48.7, 61.5, and 68° are assigned to the ($\bar{1}$11), (111), ($\bar{2}$02), ($\bar{1}$13), and (220) planes of monoclinic CuO (JCPDS no.: 080–1916). Interestingly, a diffraction peak at ~36.4° was also identified belonging to the (111) plane of cuprous oxide (Cu_2O) (JCPDS no.: 078–2076), indicating the formation of Cu^+ in the CuO_x/HfO_2 samples.

The wide-scan X-ray photoelectron spectroscopy (XPS) spectrum of the CuO_x/HfO_2 shows the predominant presence of Cu, O, and Hf elements without other impurities in the sample (Fig. S2a). Fig. 1b presents the Cu 2p XPS spectra of pure CuO and CuO_x/HfO_2, which displays a spin-orbit split doublet with Cu $2p_{1/2}$ at ~954.1 eV and $2p_{3/2}$ at 934.2 eV arising from Cu^{2+} species.[16] There also exist three apparent Cu^{2+} satellites with binding energies (BEs) at ~961.1, 942.3, and 939.9 eV. For CuO_x/HfO_2, a doublet with Cu $2p_{1/2}$ at ~952.1 eV and $2p_{3/2}$ at 932.2 eV can be deconvoluted, signifying the existence Cu^+ moieties.[6] The Cu LMM Auger excitation spectra (Fig. S2b) verified the presence of Cu^+ with a characteristic Auger peak at ~570.1 eV in CuO_x/HfO_2,[17] while no Cu^0 signal at about 568 eV was discernible. The Cu^+ content in the catalyst could be readily modulated by altering the Cu-to-Hf molar ratio (Fig. S3

[a] State Key Laboratory of Organic-Inorganic Composites, Beijing University of Chemical Technology, Beijing 100029, P. R. China. E-mail: sunzy/mail.buct.edu.cn.
[b] College of Biological, Chemical Science and Engineering, Jiaxing University, Jiaxing, Zhejiang 314001, P. R. China
[c] Department of Physics, University of Warwick, Coventry, UK
Electronic Supplementary Information (ESI) available: [Experimental and relevant

and Table S1), approaching 43.6% at the Cu-to-Hf molar ratio of 3:2. The BEs of the Hf 4f peaks in the CuO_x/HfO_2 shift markedly to higher values relative to pure HfO_2 (Fig. S4a), indicative of electron transfer from Hf to Cu resulting in the formation of Cu^+ in the hybrid. The O 1s spectra can be deconvoluted into three sub-bands (Fig. S4b) at about 532.4, 530.8, and 529.5 eV, corresponding to surface physi-/chemisorbed water, vacancy oxygen, and lattice oxygen.[6] The ratio of vacancy oxygen and lattice oxygen in CuO_x/HfO_2 was estimated to be ~0.57, over two fold that of bare CuO (~0.21) and HfO_2 (~0.18). The abundant oxygen vacancies (V_O) can boost chemical adsorption and activation of CO_2, benefiting the ECR.

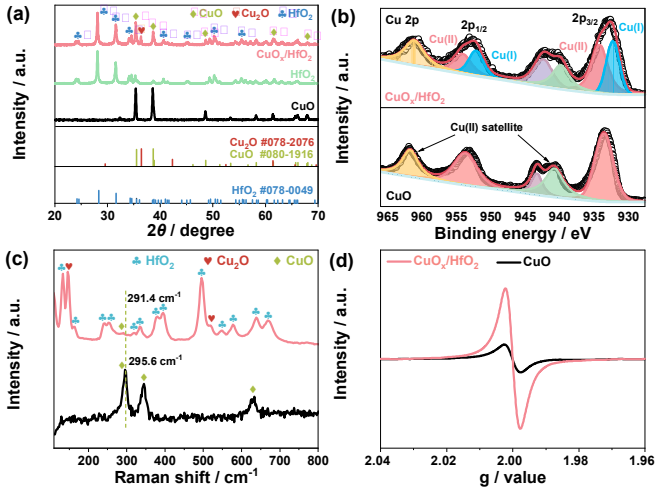

Fig. 1 (a) XRD patterns of the as-obtained CuO, HfO_2, and CuO_x/HfO_2(3:2). (b) Cu 2p XPS, (c) Raman, and (d) electron spin resonance (ESR) spectra of CuO and CuO_x/HfO_2(3:2).

Raman spectroscopy was used to detect the local structure of CuO_x/HfO_2. As illustrated in Fig. 1c, a typical A_g band at ~295.6 and two B_g modes at 345.2 and 626.7 cm^{-1} are observed for neat CuO.[18] The band at 295.6 cm^{-1} shifted to lower value of 291.4 cm^{-1} for CuO_x/HfO_2, indicating prominent interaction between the metal oxides. The peaks at ~132.6, 259.7, 383.1, 500.2, 579.4, and 670.9 cm^{-1} could be assigned to the A_g modes of HfO_2, while the vibrations found at 163.1, 242.3, 323.3, 335.2, 395.4, 548.3, and 641.3 cm^{-1} are attributed to the B_g modes of monoclinic HfO_2.[19] The two characteristic phonon frequencies at 146.1 and 520.2 cm^{-1} may correspond to the IR active F_{1u} (Γ_{15}) mode and $3\Gamma'_{25}$ (F_{2g}) band of Cu_2O.[6] Temperature-programmed reduction by hydrogen (H_2-TPR) showed two peaks at ~210.5 and 252.3 °C for CuO_x/HfO_2 (Fig. S5a), corresponding to the respective reduction of Cu^{2+} to Cu^+ and Cu^+ to Cu^0. CuO_x/HfO_2 exhibited these remarkably lower TPR temperatures compared with bare CuO due to hydrogen spillover to the cupric oxide at the composite interface. This implies that HfO_2 in proximity can help reduce CuO_x in the composite. By ESR spectroscopy, CuO_x/HfO_2 was found to display a drastically more intense symmetric pair of peaks than pure CuO with a *g* signal at 2.00 associated with trapped unpaired electrons by oxygen vacancies via adsorbed oxygen species from air (Fig. 1d), in agreement with the XPS results.[18] V_O-rich surfaces of CuO_x/HfO_2 favor CO_2 adsorption and activation and also provide strong binding affinities to *CO and *COH, but weak affinity to $*CH_2$, thus promoting catalytic turnover and the formation of C_2H_4.[20] Indeed, the CO_2 adsorption capacity of CuO_x/HfO_2 is two times that of pure CuO (Fig. 5b). The higher CO_2 uptake may be associated with the presence of more V_O (with abundant localized electrons) on CuO, a slightly larger surface area, and also the incorporation of HfO_2 with Lewis basic sites. The enhanced CO_2 adsorption facilitates enrichment of CO_2 on the local surface of the cathode and conducively accelerates catalytic turnover frequency.

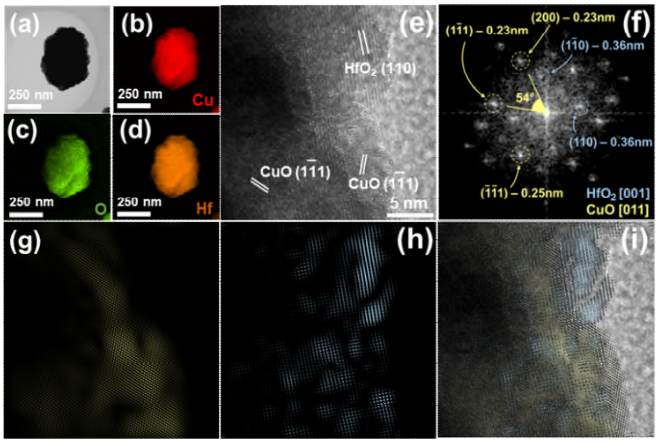

Fig. 2 (a) TEM images with corresponding EDS elemental maps of (b) Cu, (c) O, and (d) Hf. (e) High-resolution TEM image and (f) FFT of CuO_x/HfO_2(3:2) with reflections for CuO and HfO_2 labelled. The HfO_2 is oriented down the [001] zone axis and the CuO oriented down the [011]. (g, h) Reconstructed FFTs from the corresponding coloured reflections in (f), showing the spatial distribution of the two crystals in the image. (i) Overlay of g and h on e.

Microstructural characterization by scanning electron microscopy (SEM) (Fig. S6a–e) and transmission electron microscopy (TEM) (Figs. 2a and S6f) showed that the as-prepared CuO_x/HfO_2 manifests a plate-like morphology possessing sizes of 200–400 nm with rough surfaces. Energy-dispersive X-ray spectroscopy (EDS) elemental maps (Fig. 2b–d) confirmed the presence and homogeneous dispersions of Hf, Cu, and O elements across the sample. High-resolution TEM observation and fast Fourier transformation (FFT) revealed that CuO_x and HfO_2 are highly crystalline with ordered lattice fringes (Fig. 2e–i). The metal oxides are in close contact with large interface areas.

The inherent properties of CuO_x/HfO_2 for ECR were first explored in a gas-tight H-type cell containing 0.1 M $KHCO_3$ electrolyte with continuous CO_2 bubbling at ambient temperature and pressure.[6] The constitution of the gaseous and liquid products was monitored by gas chromatography (GC) and nuclear magnetic resonance (^{1}H NMR) spectroscopy, respectively. Linear sweep voltammetry (LSV) test showed larger reduction currents under a CO_2 environment than in an Ar atmosphere throughout the scanned potential range (from 0 to −1.4 V versus reversible hydrogen electrode (*vs.* RHE), all the following potentials are presented relative to the RHE scale) (Fig. 3a), indicating the occurrence of CO_2 reduction. To study the origin of ECR reactivity, the catalytic performances over CuO_x/HfO_2 with different Cu-to-Hf molar ratios were investigated. All catalysts were found to display a similar rough surface morphology and comparable average sizes, eliminating the influence of morphology and size on ECR activity (Fig. S6). The faradaic efficiency (FE) toward C_2H_4 formation increased with improving HfO_2 content from 2:1 (Cu-to-Hf) reaching a maximum at 3:2 (Figs. 3b and S7). Further increasing HfO_2 amount caused a drop of ECR activity plausibly due to less

exposed active sites of Cu. Interestingly, we found that the trend of C_2H_4 FE fits well with the alteration of Cu^+. Such a finding is in good agreement with prior observations.[21,22] The existence of Cu^+ could effectively decrease the energy barrier of *CO dimerization, in favor of C_2H_4 formation. Reduction products including CO, HCOOH, CH_4, and C_2H_4 together with H_2 were produced from −0.8 to −1.3 V for CuO and CuO_x/HfO_2, while only small amounts of HCOOH were generated on HfO_2 (Figs. 3c and S8). At potentials ≥ –0.9 V, ECR mainly produces C_1 compounds of CO and HCOOH whilst the formation of C_2H_4 begins to dominate at applied bias from –1.0 to –1.2 V, which is likely due to the generation of more CO and higher *CO coverage. At more negative potentials, larger amounts of protons are formed, resulting in boosted protonation of *CO to CH_4. The FE toward C_2H_4 generation exhibits a volcano-type correlation with the increase of overpotential, reaching the highest value at –1.1 V. Notably, throughout the applied voltages, CuO_x/HfO_2 invariably exceeds CuO in terms of both C_2H_4 FE and overall ECR FE. This emphasizes the significance of HfO_2 in combating the HER and also accelerating the coupling of adsorbed *CO to yield C_2H_4. Particularly, CuO_x/HfO_2 delivers an average overall CO_2 reduction FE of 68.6% and a C_2H_4 FE of 48.7%, about 2 and 2.5 times that of individual CuO, respectively.

The partial C_2H_4 geometric current density and C_2H_4 production rate of CuO_x/HfO_2 are ~5.7 mA cm^{-2} and 14 μmol $mg_{cat.}^{-1}$ h^{-1}, approximately 2.4 and 2.5 times that of bare CuO (Fig. S9a and b). Also, CuO_x/HfO_2 affords superior C_2H_4 selectivity (FE_{C2H4}/FE_{C1}) compared with bare CuO over a wide voltage range from −0.8 to −1.2 V (Fig. S9c). We further estimated the C_2H_4 cathodic energy efficiency (EE) based on the C_2H_4 FE and the ratio of the thermodynamics of the reaction over cell voltage (see ESI). CuO_x/HfO_2 delivers a maximal C_2H_4 EE of 27.3 ± 0.7% at a current density of 11 ± 0.9% mA cm^{-2} (Fig. S9d). Remarkably, both FE and EE toward C_2H_4 formation over CuO_x/HfO_2 surpass many prior reported Cu-based electrocatalysts under similar or larger overpotentials (Fig. S10 and Table S2). Alternated electrolysis cycling measurements between Ar- and CO_2-saturated electrolytes disclosed that the yield of C_2H_4 was maintained for at least four continuous cycles (Fig. S11). This also supports that the evolved C_2H_4 stemmed from the feed gas CO_2. Equally importantly, the CuO_x/HfO_2 catalysts present nearly unchanged current density and FE for C_2H_4 production even after 12 h of electrolysis at –1.1 V, indicating its long-term stability (Fig. 3d). Post characterization by XPS (Fig. S12), SEM (Fig. S13a), and TEM (Fig. S13b) showed that the surface concentration of Cu^+, morphology and size of CuO_x/HfO_2 were maintained after 1 h of polarization, mirroring its good stability due to the strong interplay between HfO_2 and CuO_x.

To investigate the role of the CuO-HfO_2 interface, we attempted to regulate the interfacial structure by manipulation of synthetic conditions including the feeding sequence of metal precursors. It was found that a cascade addition of the two metal precursors all led to a substantial drop of C_2H_4 FE (Table S3). Similarly, a physical mixture of CuO and HfO_2 with equivalent metal oxide contents also exhibited lower CO_2 reduction activity compared to CuO_x/HfO_2 (Fig. S14). In all cases, the accessible CuO-HfO_2 interfaces with exposed copper sites were markedly reduced, which accounted for the decreased ECR performance. Therefore, we infer that engineering the interface of CuO-HfO_2 to yield and stabilize Cu^+ is crucial to promoting the CO_2-to-C_2H_4 conversion.

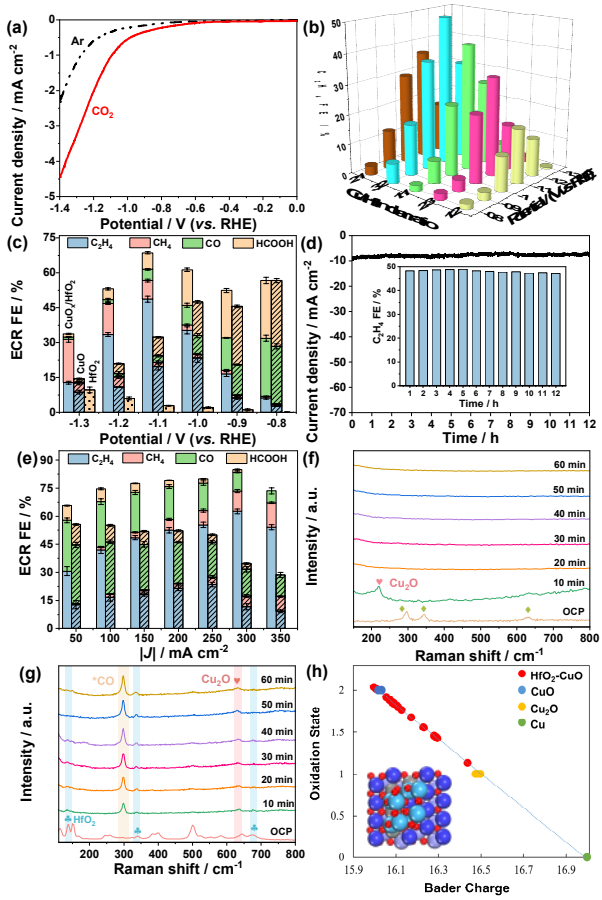

Fig. 3 (a) LSV curves of CuO_x/HfO_2 in an H-type cell with 0.1 M Ar- (dashed line) or CO_2- (solid line) saturated $KHCO_3$. (b) C_2H_4 FE on CuO_x/HfO_2 with different Cu-to-Hf molar ratios at various applied potentials. (c) ECR FEs over CuO (striped column), HfO_2 (dotted column), and CuO_x/HfO_2(3:2) at distinct potentials. (d) Current density versus electrolysis time over CuO_x/HfO_2(3:2). The inset displays the respective C_2H_4 FE-time response. (e) ECR FEs of CuO_x/HfO_2(3:2) and bare CuO at geometric current densities from 50 to 350 mA cm^{-2} in a flow cell. Operando Raman spectra of (f) CuO and (g) CuO_x/HfO_2(3:2) versus ECR reaction time at –1.1 V. (h) Oxidation states of surface Cu derived by Bader charge investigation. The inset shows the top view of the optimized geometries of CuO_x/HfO_2. Bule and grey (adjacent to Hf atom) colors represent Cu atoms while sky blue and red colors correspond to Hf and O atoms, respectively.

The Tafel slope of CuO_x/HfO_2 was calculated to be 154.5 mV dec^{-1} (Fig. S15a), smaller than that of pure CuO (164.3 mV dec^{-1}), indicating favourable kinetics for ECR over the composite catalyst. Alternatively, Nyquist plot analysis (Fig. S15b) showed lower charge transfer resistance for CuO_x/HfO_2 compared to pure CuO and HfO_2, reflecting faster interfacial charge transfer between the working electrode and reactants in the electrolyte to facilitate the CO_2 conversion. In addition, CuO_x/HfO_2 exhibited a slightly larger electrochemical active surface area (derived from measurement of double layer capacitance) than pure CuO and HfO_2 (Fig. S16), conducive to the ECR. We further performed ECR using a three-compartment flow cell electrolyzer with gas-diffusion layers to circumvent the issue of low solubility of CO_2 in aqueous electrolytes. As illustrated in Figs. 3e and S17, the C_2H_4 FE was further improved to 62.6 ± 1.3% with a total ECR FE of up to 84.9 ± 0.3% at a geometric current density of 300 mA cm^{-2} in 1 M KOH solution, comparable to

many previous reported Cu-based materials in flow cells (Table S4). This is in stark contrast to pure CuO with a C_2H_4 of 11.6 ± 1.6% and overall ECR FE of 34.7 ± 0.5%.

We performed CO_2 and CO-TPD measurements to gain a mechanical understanding of the enhanced activity. CuO_x/HfO_2 was observed to exhibit a substantially higher CO_2 chemical desorption peak (412.1 °C) than pure CuO (252.5 °C) (Fig. S18a), implying larger CO_2 binding strength at the interface of CuO_x and HfO_2. Similarly, the CO desorption peak for CuO_x/HfO_2 approaches 354.4 °C exceedling that of 284.9 °C for CuO, as shown in Fig. S18b, suggesting a much stronger CO binding energy on the metal oxide composite. As a consequence, we conclude that the introduction of HfO_2 greatly enhanced the CO_2 and CO adsorption on CuO_x surface. The association of strong CO binding is believed to be the active sites for C–C coupling. Moreover, we conducted CO electroreduction measurements in H-cells with 0.1 M KOH as cathodic electrolyte (Fig. S19). CuO_x/HfO_2 started to form C_2H_4 at –0.3 V and attained a maximal C_2H_4 FE of 50.5 ± 1.7% (at –0.4 V), whereas bare CuO did not yield C_2H_4 at potentials more positive than –0.4 V. This further validates that the CuO_x/HfO_2 interface can efficiently catalyze C–C coupling reactions at low overpotentials. Furthermore, operando Raman spectroscopy measurements were carried out to detect reaction intermediates and catalyst structural alteration during CO_2 reduction. In contrast to absence of peaks for pure CuO after 10 min of CO_2 electrolysis (Fig. 3f), a prominent band located at ~299.7 cm^{-1} appeared on CuO_x/HfO_2 which became gradually stronger with polarization time (Fig. 3g). The peak is associated with the frustrated rotation of *CO bound to Cu_2O in an atop geometry, which locally protected Cu^+ sites against further reduction.[23] This provides an evidence that the incorporated Hf species facilitate strong *CO binding and high *CO coverage, contributing to the enhanced C–C coupling activity. Bader charge analysis by density functional theory calculations showed that the oxidation states of some Cu atoms at the CuO-HfO_2 interface fall between that of Cu_2O and CuO (Fig. 3h), illustrating that the interfacial HfO_2 cluster altered the oxidation state of adjacent Cu atoms in CuO toward that of Cu_2O. This is in accordance with the above XRD, XPS, and TPR results, verifying the existence of Cu^+ in CuO_x/HfO_2, and that HfO_2 plays a central role in stabilizing Cu^+.

In summary, we have demonstrated that tuning of the CuO_x/HfO_2 interface can greatly boost CO_2 adsorption and binding of *CO, thus facilitating tandem dimerization and protonation to produce C_2H_4 via ECR. The designed metal oxide composite imparted a remarkable FE toward C_2H_4 formation, reaching 62.6 ± 1.3%, and with an overall CO_2 reduction FE of 84.9 ± 0.3% at a high current density of 300 mA cm^{-2}, over five-fold that of pure CuO and also outperforming prior reported Cu-based electrocatalysts. Tailoring the level of HfO_2 incorporation enables fine-tuning of the ECR activity and also impedes the competing HER. The activity of the catalyst maintains good stability even after consecutive polarization for 12 h. The existence of Cu^+ species was confirmed by XRD, XPS, TPR, and Bader charge analysis. Operando Raman spectroscopy measurements corroborate that the introduction of HfO_2 significantly strengthened *CO binding and coverage, thus improving C–C coupling activity. This work offers a simple and effective avenue to enhancing the ECR to yield C_2H_4.

This work was supported by the National Natural Science Foundation of China (No. 21972010) and Beijing Natural Science Foundation (No. 2192039).

Conflicts of interest

The authors declare no conflicts of interest.

Notes and references

1 J. M. Chen, *The Innovation,* 2021, **2**, 1–2.
2 L. Fan, C. Xia, F. Yang, J. Wang, H. Wang and Y. Lu, *Sci. Adv.*, 2020, **6**, eaay3111.
3 M. Jia, C. Choi, T. -S. Wu, C. Ma, P. Kang, H. Tao, Q. Fan, S. Hong, S. Liu, Y. -L. Soo, Y. Jung, J. Qiu and Z. Sun, *Chem. Sci.*, 2018, **9**, 8775–8780.
4 H. Tao, X. Sun, S. Back, Z. Han, Q. Zhu, A. W. Robertson, T. Ma, Q. Fan, B. Han, Y. Jung and Z. Sun, *Chem. Sci.*, 2018, **9**, 483–487.
5 L. Hao and Z. Sun, *Acta Phys. -Chim. Sin.*, 2021, **37**, 2009033.
6 S. Chu, X. Yan, C. Choi, S. Hong, A. W. Robertson, J. Masa, B. Han, Y. Jung and Z. Sun, *Green Chem.*, 2020, **22**, 6540–6546.
7 R. He, A. Zhang, Y. Ding, T. Kong, Q. Xiao, H. Li, Y. Liu and J. Zeng, *Adv. Mater.*, 2018, **30**, 1705872.
8 T. Zhuang, Z. Liang, A. Seifitokaldani, Y. Li, P. De Luna, T. Burdyny, F. Che, F. Meng, Y. Min, R. Quintero-Bermudez, C. T. Dinh, Y. Pang, M. Zhong, B. Zhang, J. Li, P. Chen, X. Zheng, H. Liang, W. Ge, B. Ye, D. Sinton, S. Yu, E. H. Sargent, *Nat. Catal.*, 2018, **1**, 421–428.
9 L. Wang, X. Li, L. Hao, S. Hong, A. W. Robertson and Z. Sun, *Chin. J. Catal.*, 2022, **43**, 1049–1057.
10 F. Li, G. H. Gu, C. Choi, P. Kolla, S. Hong, T. -S. Wu, Y. -L. Soo, J. Masa, S. Mukerjee, Y. Jung, J. Qiu and Z. Sun, *Appl. Catal. B Environ.*, 2020, **277**, 119241.
11 M. Jia, Q. Fan, S. Liu, J. Qiu and Z. Sun, *Curr. Opin. Green Sustain. Chem.*, 2019, **16**, 1–6.
12 M. Jia, S. Hong,T. -S. Wu, X. Li, Y. -L. Soo and Z. Sun, *Chem. Commun.*, 2019, **55**, 12024–12027.
13 Q. Chang, J. H. Lee, Y. Liu, Z. Xie, S. Hwang, N. S. Marinkovic, A. A. Park, S. Kattel and J. G. Chen, *JACS Au*, 2022, **2**, 214–222.
14 W. Ma, X. He, W. Wang, S. Xie, Q. Zhang and Y. Wang, *Chem. Soc. Rev.*, 2021, **50**, 12897–12914.
15 Q. Fan, M. Zhang, M. Jia, S. Liu, J. Qiu and Z. Sun, *Mater. Today Energy*, 2018, **10**, 280–301.
16 S. Chu, S. Hong, J. Masa, X. Li and Z. Sun, *Chem. Commun.*, 2019, **55**, 12380–12383.
17 Q. Fan, X. Zhang, X. Ge, L. Bai, D. He, Y. Qu, C. Kong, J. Bi, D. Ding, Y. Cao, X. Duan, J. Wang, J. Yang and Y. Wu, *Adv. Energy Mater.*, 2021, **11**, 2101424.
18 Y. Jiang, C. Choi, S. Hong, S. Chu, T. -S. Wu, Y. -L. Soo, L. Hao, Y. Jung and Z. Sun, *Cell Rep. Phys. Sci.*, 2021, **2**, 100356.
19 A. Ramadoss and S. J. Kim, *J. Alloys Comp.*, 2012, **544**, 115–119.
20 Z. Geng, X. Kong, W. Chen, H. Su, Y. Liu, F. Cai, G. Wang and J. Zeng, *Angew. Chem. Int. Ed.*, 2018, **57**, 6054–6059.
21 R. M. Arán-Ais, F. Scholten, S. Kunze, R. Rizo and B. R.Cuenya, *Nat. Energy*, 2020, **5**, 317–325.
22 W. Christina, X. Li, W. Matthew and G. Kanan, *J. Am. Chem. Soc.*, 2012, **134**, 7231–7234.
23 H. Sun, L. Chen, L. Xiong, K. Feng, Y. Chen, X. Zhang, X. Yuan, B. Yang, Z. Deng, Y. Liu, M. H. Rümmeli, J. Zhong, Y. Jiao and Y. Peng, *Nat. Commun.*, 2021, **12**, 6823.

